2023 IEEE 20th International Symposium on Biomedical Imaging (ISBI) | 978-1-6654-7358-3/23/$31.00 ©2023 IEEE | DOI: 10.1109/ISBI53787.2023.10230394

PROBING INTRACELLULAR ELASTICITY WITH MINIMAL-HESSIAN REGISTRATION

Yekta Kesenci[1,*], *Aleix Boquet-Pujadas*[2,*], *Michael Unser*[2], *Jean-Christophe Olivo-Marin*[1]

[1] Institut Pasteur, Université Paris Cité, CNRS UMR 3691, BioImage Analysis Unit, F-75015 Paris, France.

[2] Biomedical Imaging Group, École polytechnique fédérale Lausanne (EPFL), Lausanne, Switzerland.

ABSTRACT

We propose an image-based elastography method to measure the heterogeneous stiffness inside a cell and its nucleus. It uses a widely accessible setup consisting of plate compression imaged with fluorescence microscopy. Our framework recovers a spatial map of Young's modulus from images of the intracellular displacements. These displacements are measured with a novel optical-flow technique characterised by a Hessian-Schatten norm regularizer. The aim is to favor piecewise-linear displacements because they reproduce solutions to linear elasticity problems well when the underlying modulus is piecewise-constant, as is often the case in cells. Our computational approach is fast enough for long time-lapse acquisitions and 3D imaging. It is able to cope with two common pitfalls of biological elastography: high compressibility and small compressions to avoid damage. We show our method is faster and more accurate than the state-of-the-art.

***Index Terms*—** Nuclear mechanics, elastography, optical flow, nuclear norm

1. INTRODUCTION

The stiffness of the cell nucleus is an important marker for diseases as diverse as Emery-Dreifuss muscular dystrophy, Hutchinson-Gilford progeria syndrome, or cancer [1]. To measure stiffness, biologists perform a simple tensile test [2], [3]. They apply a known force on the nuclear surface, for example with an atomic-force microscope, and measure how much the length or perimeter of the nucleus changes. A single figure of merit—a constant Young's modulus E—is then derived from the shape measurement using analytical versions of Hooke's law in some characteristic dimension [4]. While the experimental setup and the measurements themselves are convenient, these methods oversimplify the composition and geometry of the nucleus and the physical relationship with the elasticity modulus, reducing the description of the process to a single number and also ignoring any cellular material between the probe and the nucleus. In order to deform the nucleus enough, the practitioner has to significantly squeeze the cytoskeleton at the risk of compromising the cell's integrity. Such an extreme handling is required to overcome the limitations in the imaging process.

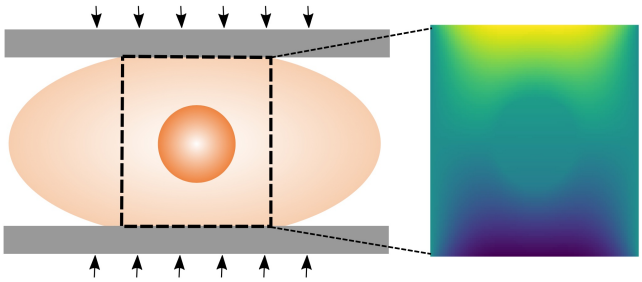

Fig. 1: Experimental setting. A plate compression of a cell (left) is imaged to measure the displacements (right) that are later inverted to recover stiffness.

By contrast, medical elastography has long relied on ultrasound imaging to detect stiff inclusions in the body—tumors for example—with its resolution being better matched to the human scale [5]. To this end, a light mechanical stress is applied on the tissue, either as a static compression or dynamically in the form of pressure waves. In the former case, one then applies registration techniques to estimate the deformation fields. These have enough resolution to drive a reconstruction algorithm that ultimately yields a map of Young's modulus.

Only recently has microscopy improved enough to allow the use of similar techniques in biological settings. For example, [6] applies a dynamical tension on cells to measure their elasticity at the cost of a complex setup, whereas [7] leverages the natural compressions of the cell. The latter, however, can only extract dimensionless maps and at limited speed. Interestingly, imaging resolution has also increased in the traditional setting of nuclear probing described above [8], [9]. The result are fluorescent images with rich texture. We propose to harness this experiment to measure spatial elasticity maps $E(\mathbf{r})$ from very small static compressions that preserve the cell's integrity (Figure 1). To this end, we first need to estimate the deformation from the images.

Optical flow has been used to compute tissue strain in multiple medical imaging applications [10]. The most popular among such OF methods is based on vectorial total variation (TV-L_1) [11]. However OF by itself is not accurate

∗ These authors contributed equally to this work.

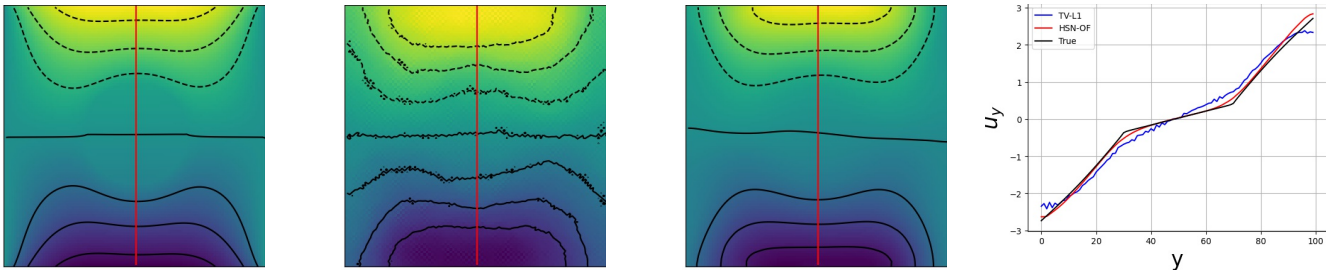

True TV-L_1 HSN-OF Profile

Fig. 2: Axial displacements in a plate-compression experiment. The Hessian-Shatten-Norm regularization (HSN-OF) enforces piecewise-linear displacements, removing the staircasing effect. The profile is taken over the red line.

enough to estimate the fine lateral displacements required to reconstruct sensitive stiffness maps under small compressions. To overcome this limitation, most elastography methods preprocess the displacement field "before inverting" for Young's modulus, for example by assuming incompressibility of the tissue [12]. Unfortunately, these approaches are not applicable in biology because cells and their nuclei are highly compressible. Instead of preprocessing, other methods resort to complex optimization schemes to stabilise the elasticity map [13], but their computational complexity is unfit for the long acquisitions required to study cell migration [14] and do not scale well to 3D.

We argue that the regularisation term of OF must be chosen carefully. In particular, the piecewise constant displacements enforced by the traditional choice of vectorial total variation (TV-L_1) method introduce errors in the derivatives when the strain is computed. These errors are then amplified when computing Young's modulus from the strain. To mitigate these effects in a way that is both fast and compatible with biological experiments, we propose to regularise OF with a second-order term based on the Hessian Schatten norm [15]. By favoring piecewise linear displacements, subsequent differentiation becomes more robust and allows for fast reconstruction methods such as [16]. Moreover, in the linear regime of cell-safe experiments, solutions to the elasticity equations tend to be piecewise linear when the underlying modulus is piecewise constant (Figure 2). In fact, they are exactly piecewise linear in the direction of traction when the boundaries are free. As a result, the method is not only stable against variations in the boundary forces and the sizes of the nucleus, but also more accurate than other reconstruction frameworks applied to displacements computed with OF techniques.

2. METHOD

2.1. Mechanical Model of the Cell

We consider the cell and the nucleus as continuous media in a compact domain Ω. We consider that the applied forces are small, which is compatible with the protection of the cellular integrity. Further we assume that these forces are applied slowly enough to avoid triggering the viscous properties of the cell. Under these conditions, the cell and the nucleus can be represented as a linearly isotropic elastic material that obeys to:

$$\begin{cases} \nabla \cdot \varsigma = 0, & \text{in } \Omega \\ \varepsilon(\mathbf{u}) = \lambda \operatorname{Tr}(\varepsilon(\mathbf{u}))\mathbb{1} + 2\mu\varepsilon(\mathbf{u}), & \text{in } \Omega \\ \varepsilon(\mathbf{u}) = \frac{1}{2}(\nabla\mathbf{u} + \nabla\mathbf{u}^{\mathrm{T}}), & \text{in } \Omega \\ \mathbf{u} = \mathbf{g}, & \text{on } \Gamma_{\mathbf{g}} \\ \varsigma \cdot \mathbf{n} = \mathbf{T}, & \text{on } \Gamma_{\mathbf{T}}, \end{cases} \tag{1}$$

where $\varsigma : \Omega \to \mathbb{R}^2 \times \mathbb{R}^2$ and $\varepsilon : \Omega \to \mathbb{R}^2 \times \mathbb{R}^2$ are the second-order stress and strain tensors, $\mathbf{u}$ the displacement field, λ and μ the Lamé parameters, $\mathbf{g}$ and $\mathbf{T}$ the displacements and applied tractions on the boundary, and $\mathbf{n}$ the vector that is normal to the boundary $\partial\Omega = \Gamma_{\mathbf{g}} \cup \Gamma_{\mathbf{T}}$ of the domain [4]. The Lamé parameters are expressed using Young's modulus (E) and Poisson's ratio (ν) through the relations $\lambda = \frac{E\nu}{(1+\nu)(1-2\nu)}$ and $\mu = \frac{E}{2(1+\nu)}$. We consider $E(\mathbf{r})$, $\mathbf{r} \in \Omega$, to vary across the domain.

2.2. Estimation of Displacements from Images

Denoting by $I : \Omega_I \times \mathbb{R}_{\geq 0} \to \mathbb{R}_{\geq 0}$ the intensity function of the images, OF methods estimate a displacement field $\mathbf{u}_{OF}$ by solving the variational problem

$$\mathbf{u}_{OF} = \underset{\mathbf{u}}{\operatorname{argmin}} \left(\int_{\Omega_I} \left(\frac{\partial I}{\partial t} + \mathbf{u} \cdot \nabla I \right)^2 + \alpha R(\mathbf{u}) \right), \tag{2}$$

where $\Omega_I \subset \Omega$ is the domain of the image, $\alpha \in \mathbb{R}_{>0}$ a regularization constant, and R the regularization functional [17]. This is consistent with the assumptions of brightness constancy and small displacements which are made in reason of the stability of fluorescent markers and the small intensity of the stress applied on the boundary, respectively. The first term in (2) is the data-fidelity one. It promotes displacements that properly deform the initial image onto the second one. The regularization term in (2) addresses the well-known aperture problem.

Two common choices for R include the L_2 norm of the Jacobian of the displacement field [17] and its TV-L_1 [11]. The

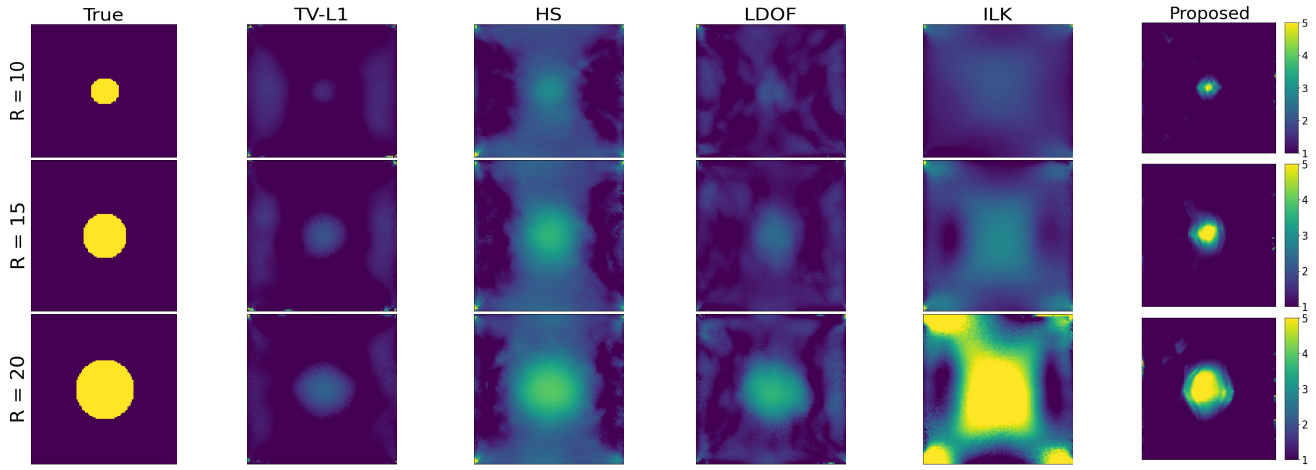

Fig. 3: Young's modulus reconstruction of the contending methods for varying radii.

former often provides solutions that are too smooth, whereas the latter is good at restoring vector fields with sharp edges but suffers from staircasing because it favors piecewise-constant solutions. Due to the differentiation step in the reconstruction procedure, the displacements resulting from TV-L_1 yield highly oscillatory strain components, in contradiction with the expectation that the constant traction on the boundaries ought to produce a smooth stress over the domain (1), while being at the same time linearly dependent on ε and E.

To better inform our solver, we promote piecewise linear displacements. As compared to TV-L_1, ours are smoother and better resemble solutions to the linearly elastic equations under a piecewise-constant modulus. We propose to equip the optical-flow problem with the regularisation term

$$R(\mathbf{u}) = \int_{\mathbf{r}\in\Omega_I} \left(||\mathscr{H}\{\mathbf{u}_\mathrm{x}\}(\mathbf{r})||_{S_1} + ||\mathscr{H}\{\mathbf{u}_\mathrm{y}\}(\mathbf{r})||_{S_1} \right) d\mathbf{r}, \quad (3)$$

where $\mathscr{H}$ denotes the Hessian operator, $\mathbf{u}_\mathrm{x}$ and $\mathbf{u}_\mathrm{y}$ the components of the displacement field and $||\cdot||_{S_1}$ the Schatten 1-norm defined for a matrix $\mathbf{X}$ with singular values σ_k as

$$||\mathbf{X}||_{S_1} \triangleq \sum_k |\sigma_k|. \quad (4)$$

The minimisation of the Schatten 1-norm tends to sparsify the principal curvatures of the displacement, encouraging piecewise linear solutions. In practice, we compute a discrete approximation of (3). We first compute a finite-difference approximation $\mathbf{H}_\mathrm{x}, \mathbf{H}_\mathrm{y} \in \mathbb{R}^{2\times 2}$ of the Hessians using each component at every point of the $(N_\mathrm{x} \times N_\mathrm{y})$ pixel grid. We then take the ℓ_1 norm of $||\mathbf{H}_\mathrm{x}||_{S_1} + ||\mathbf{H}_\mathrm{y}||_{S_1}$ over all points.

The problem in (2) is convex. We solve it by accelerated proximal gradient descent (APGD) [18]. The gradient is computed directly from the OF term, whereas the proximal operator of the Hessian's Schatten norm is computed with a fast iterative shrinkage-thresholding algorithm with early stopping (50 iterations). Since (3) is separable, the proximal can be evaluated independently for each of the two parts and later combined together.

The step size for the outer APGD algorithm is chosen as the inverse of the Lipschitz constant of the gradient of the data term F in (2). Let $\mathbf{u}_1$, $\mathbf{u}_2$ be two displacement fields, $\mathbf{J}_1 = \left(\nabla_x I^2, \nabla_x I \nabla_y I\right)^T$, $\mathbf{J}_2 = \left(\nabla_x I \nabla_y I, \nabla_y I^2\right)^T$, and $||\cdot||$ the Frobenius norm. The Lipschitz constant is provided by the Cauchy-Schwarz inequality as:

$$||\nabla F(\mathbf{u}_1) - \nabla F(\mathbf{u}_2)|| \leq 2\sqrt{||\mathbf{J}_1||^2 + ||\mathbf{J}_2||^2}||\mathbf{u}_1 - \mathbf{u}_2|| \quad (5)$$

2.3. Reconstruction of Stiffness from Displacements

We consider two reconstructions of Young's modulus from a displacement field: direct, and indirect.

2.3.1. *Direct Methods*

Direct reconstructions mesh the image domain into N_e rectangular elements with the $(N_\mathrm{x} \times N_\mathrm{y})$ pixels as nodes. By discretizing the problem in a finite-elements basis, it can be shown that (1) can be formulated as the linear system $\mathbf{De} = \mathbf{t}$. Here, $\mathbf{e}$ is the vector containing the Young's modulus of each element, $\mathbf{t}$ is the vector corresponding to the traction, and $\mathbf{D}$ is a $(2N_\mathrm{x}N_\mathrm{y} \times N_\mathrm{e})$ sparse matrix that depends on the estimated displacements $\mathbf{u}_\mathrm{OF}$, on Poisson's ratio ν, and on the dimension of each element [16]. Since the matrix $\mathbf{D}$ is very sparse, this system of equations can be inverted very efficiently. However, this method suffers from poor conditioning. It may yield spurious reconstructions of Young's modulus if the displacement field is inaccurate.

2.3.2. *Indirect Methods*

Indirect methods aleviate this conditioning problem by solving the PDE-constrained optimization problem

$$\underset{E}{\text{argmin}} \quad J(\mathbf{u}, E) = \int \left(||\mathbf{u} - \mathbf{u}_\mathrm{OF}||^2 + \beta ||E||^2 \right) d\Omega,$$
$$\text{s.t.} \qquad \text{Eq. (1)}, \quad (6)$$

Experiment 1	NRMSE	SR	CNR	Runtime (s)	**Experiment 2**	NRMSE	SR	CNR	Runtime (s)
Proposed	$\mathbf{19.12 \pm 0.65}$	$\mathbf{7.77 \pm 0.22}$	5.86 ± 1.46	$\mathbf{5.62 \pm 0.27}$	**Proposed**	$\mathbf{22.27 \pm 3.67}$	$\mathbf{7.80 \pm 0.74}$	6.68 ± 1.75	$\mathbf{5.61 \pm 0.20}$
TV-L_1 + Indirect	25.92 ± 1.74	1.71 ± 0.35	3.44 ± 1.54	301 ± 181	TV-L_1 + Indirect	31.50 ± 3.68	1.62 ± 0.30	4.05 ± 1.49	243 ± 176
ILK + Indirect	29.22 ± 5.46	1.63 ± 0.27	5.87 ± 1.29	201 ± 110	ILK + Indirect	32.99 ± 10.69	1.58 ± 0.17	6.16 ± 1.28	144 ± 35
LDOF + Indirect	22.51 ± 1.97	1.60 ± 0.24	9.17 ± 3.59	151 ± 73	LDOF+ Indirect	27.82 ± 3.25	1.52 ± 0.26	5.58 ± 3.59	146 ± 100
HS + Indirect	21.10 ± 0.57	2.15 ± 0.19	$\mathbf{13.26 \pm 1.41}$	146 ± 57	HS+ Indirect	23.29 ± 3.04	2.27 ± 0.11	$\mathbf{12.88 \pm 2.04}$	263 ± 222

Table 1: Mean and standard deviation of the accuracy of the reconstruction for each evaluation metric.

where $\beta \in \mathbb{R}_{>0}$ is a regularization parameter. These methods can also include the OF term directly in the variational form [19], [20]. Given a stiffness map $E(\mathbf{r})$, the finite-elements method then yields a variational form of (1) for $\mathbf{u}$. As such, J is implicitly defined as a function of E alone, which turns the constrained problem into an unconstrained one. To solve it, we use a quasi-Newton gradient-descent algorithm where the gradient is computed using the adjoint method to avoid expensive computations. The resulting Young's modulus is much less susceptible to inaccuracies in $\mathbf{u}_{\mathrm{OF}}$ because the norm of E is regularized. This comes, however, at a higher computational cost.

3. EXPERIMENTS AND RESULTS

Our claim is that OF regularized with the Hessian-Schatten norm is accurate enough to feed into a direct method. Hereafter, we refer to the combination of the two as *Proposed*. Combinations of other OF methods with indirect approaches are used for comparison.

Data Generation. We simulate a cell under plate compression (Figure 1). We consider (100×100) images of the cellular domain. Poisson's ratio ν is set to 0.33, indicating that we take the material to be compressible. We model the nucleus as a disk that accounts for 10% to 30% of the surface of the cell [21]. We ascribe a dimensionless stiffness of 1 to the cytoplasm and a stiffness of 5 to the nucleus (Figure 3) [21]. This could also represent any potential granularity inside the nucleus if the whole image was considered as the nucleus. Constant and uniform traction is applied on the upper and lower part of the image (Figure 1). For each boundary-traction value and each radius of the nucleus, a variational formulation of (1) is solved for the displacements using the finite-elements method. The resulting displacements are used to create a deformed image by warping the initial one with bicubic interpolation. These two images, along with the traction on the boundaries, are used to reconstruct Young's modulus and evaluate our method.

Evaluation Method. We denote E_{c} and E_{n} the evaluated stiffness over the cytoskeletal and nuclear domains, respectively, $\overline{E_{\mathrm{c}}}, \overline{E_{\mathrm{n}}}$ their mean value, and σ_{c}, σ_{n} their standard deviation. We evaluate the performance of our method with four metrics: the root-mean-square error normalized over the maximum of the true stiffness (NRMSE), the contrast-to-noise ratio $\mathrm{CNR} = \sqrt{2(\overline{E_{\mathrm{c}}} - \overline{E_{\mathrm{n}}})^2/(\sigma_{\mathrm{c}}^2 + \sigma_{\mathrm{n}}^2)}$, the signal ratio $\mathrm{SR} = \frac{\overline{E_{\mathrm{n}}}}{\overline{E_{\mathrm{c}}}}$, and the runtime of the reconstruction. Regarding the estimation of displacements, we challenge our method with the most popular OF methods used in biology: Horn and Schunck (HS) [17], TV-L_1 [11], large-displacement optical flow (LDOF) [22], and iterative Lukas-Kanade (ILK) [23]. The TV-L_1 and ILK implementations were taken from scikit-image, the other methods were reimplemented as per the references. Since the direct-reconstruction method collapses entirely when paired with any of these (data not shown), we only pair them with the indirect-reconstruction method. We implement it with the dolfin-adjoint library [24].

Experiment 1. We compare accuracy versus the boundary traction $||\mathbf{T}|| \in \{0.03, 0.0325, ..., 0.0375\}$ with a fixed nuclear radius of 20 (Table 1). Our method runs faster than the others by two orders of magnitude. Note that this is mainly because the quality of the proposed OF enables the use of the direct method. Its computation time (2.42 ± 0.13s) is comparable to that of the other OF methods (e.g., 2.07 ± 0.11s for TV-L_1). Our proposed method is also more accurate both in NRSME and SR, and achieves great contrast (Figure 3). However, its CNR is poorer than that of some of the competing methods because the regularization of E in the indirect method imposes a low variance on the reconstruction. In return, the results of the other methods greatly underestimate the magnitude of the modulus. As expected, TV-L_1 does a better job at preserving the edges of the displacement than the L_2 norm in HS (Figure 3). Finally, the linearity enforced by our method captures the behavior of the elasticity equation better (Figure 2).

Experiment 2. We set the traction to $||\mathbf{T}|| = 0.0375$, and simulate compression with the radius $R \in \{20, 22.5, ..., 30\}$. The conclusions are the same in terms of accuracy and performance as in Experiment 1 (Table 1). We see, however, that the TV-L_1, ILK, and LDOF methods paired with an indirect-reconstruction method are much more sensitive to the size of the nucleus, while the accuracy of our method does not vary significantly. This accuracy is maintained for smaller nuclei too (Figure 3).

4. CONCLUSION

We here presented an image-based quasi-static elastography method to compute intracellular stiffness. The framework operates fast enough to be adapted for long acquisitions or 3D reconstruction. It was shown to be more accurate than more robust reconstruction methods applied to state-of-the-art optical-flow. The framework can be easily implemented on GPU for realtime applications.

5. COMPLIANCE WITH ETHICAL STANDARDS

This is a numerical simulation study for which no ethical approval was required.

6. ACKNOWLEDGMENTS

This work was funded by the TOXONUC project (ANR-19-CE13-0034-02) and partially supported by grants from the Labex IBEID (ANR-10-LABX-62-IBEID), France-BioImaging infrastructure (ANR-10-INBS-04). The authors have no relevant financial or non-financial interests to disclose.

7. REFERENCES

[1] J. Lammerding, "Mechanics of the nucleus," *Comprehensive physiology*, vol. 1, no. 2, p. 783, 2011.

[2] M. Knight, J. van de Breevaart Bravenboer, D. Lee, G. Van Osch, H. Weinans, and D. Bader, "Cell and nucleus deformation in compressed chondrocyte–alginate constructs: Temporal changes and calculation of cell modulus," *Biochimica et Biophysica Acta (BBA)-General Subjects*, vol. 1570, no. 1, pp. 1–8, 2002.

[3] C. L. Gilchrist, S. W. Witvoet-Braam, F. Guilak, and L. A. Setton, "Measurement of intracellular strain on deformable substrates with texture correlation," *Journal of biomechanics*, vol. 40, no. 4, pp. 786–794, 2007.

[4] C. M. Hobson, M. R. Falvo, and R. Superfine, "A survey of physical methods for studying nuclear mechanics and mechanobiology," *APL bioengineering*, vol. 5, no. 4, p. 041 508, 2021.

[5] R. M. Sigrist, J. Liau, A. El Kaffas, M. C. Chammas, and J. K. Willmann, "Ultrasound elastography: Review of techniques and clinical applications," *Theranostics*, vol. 7, no. 5, p. 1303, 2017.

[6] P. Grasland-Mongrain, A. Zorgani, S. Nakagawa, *et al.*, "Ultrafast imaging of cell elasticity with optical microelastography," *Proceedings of the National Academy of Sciences*, vol. 115, no. 5, pp. 861–866, 2018.

[7] S. Ghosh, V. C. Cuevas, B. Seelbinder, and C. P. Neu, "Image-based elastography of heterochromatin and euchromatin domains in the deforming cell nucleus," *Small*, vol. 17, no. 5, p. 2 006 109, 2021.

[8] C. M. Hobson, M. Kern, E. T. O'Brien III, A. D. Stephens, M. R. Falvo, and R. Superfine, "Correlating nuclear morphology and external force with combined atomic force microscopy and light sheet imaging separates roles of chromatin and lamin a/c in nuclear mechanics," *Molecular biology of the cell*, vol. 31, no. 16, pp. 1788–1801, 2020.

[9] A. Boquet-Pujadas and J.-C. Olivo-Marin, "Multiple variational image assimilation for accessible micro-elastography," in *Journal of Physics: Conference Series*, IOP Publishing, vol. 1131, 2018, p. 012 014.

[10] R. L. Maurice, M. Daronat, J. Ohayon, E. Stoyanova, F. S. Foster, and G. Cloutier, "Non-invasive high-frequency vascular ultrasound elastography," *Physics in Medicine & Biology*, vol. 50, no. 7, p. 1611, 2005.

[11] J. S. Pérez, E. Meinhardt-Llopis, and G. Facciolo, "Tv-l1 optical flow estimation," *Image Processing On Line*, vol. 2013, pp. 137–150, 2013.

[12] X. Pan, K. Liu, J. Bai, and J. Luo, "A regularization-free elasticity reconstruction method for ultrasound elastography with freehand scan," *Biomedical engineering online*, vol. 13, no. 1, pp. 1–17, 2014.

[13] A. A. Oberai, N. H. Gokhale, and G. R. Feijóo, "Solution of inverse problems in elasticity imaging using the adjoint method," *Inverse problems*, vol. 19, no. 2, p. 297, 2003.

[14] A. Boquet-Pujadas, J.-C. Olivo-Marin, and N. Guillén, "Bioimage analysis and cell motility," *Patterns*, vol. 2, no. 1, p. 100 170, 2021.

[15] S. Lefkimmiatis, J. P. Ward, and M. Unser, "Hessian schatten-norm regularization for linear inverse problems," *IEEE transactions on image processing*, vol. 22, no. 5, pp. 1873–1888, 2013.

[16] Y. Zhu, T. J. Hall, and J. Jiang, "A finite-element approach for young's modulus reconstruction," *IEEE transactions on medical imaging*, vol. 22, no. 7, pp. 890–901, 2003.

[17] B. K. Horn and B. G. Schunck, "Determining optical flow," *Artificial intelligence*, vol. 17, no. 1-3, pp. 185–203, 1981.

[18] A. Beck and M. Teboulle, "Fast gradient-based algorithms for constrained total variation image denoising and deblurring problems," *IEEE transactions on image processing*, vol. 18, no. 11, pp. 2419–2434, 2009.

[19] A. Boquet-Pujadas and J.-C. Olivo-Marin, "Reformulating optical flow to solve image-based inverse problems and quantify uncertainty," *IEEE Transactions on Pattern Analysis and Machine Intelligence*, 2022.

[20] A. Boquet-Pujadas, T. Feaugas, A. Petracchini, *et al.*, "4d live imaging and computational modeling of a functional gut-on-a-chip evaluate how peristalsis facilitates enteric pathogen invasion," *Science Advances*, 2022.

[21] M. D. Huber and L. Gerace, "The size-wise nucleus: Nuclear volume control in eukaryotes," *The Journal of cell biology*, vol. 179, no. 4, pp. 583–584, 2007.

[22] T. Brox and J. Malik, "Large displacement optical flow: Descriptor matching in variational motion estimation," *IEEE transactions on pattern analysis and machine intelligence*, vol. 33, no. 3, pp. 500–513, 2010.

[23] A. Plyer, G. Le Besnerais, and F. Champagnat, "Massively parallel lucas kanade optical flow for real-time video processing applications," *Journal of Real-Time Image Processing*, vol. 11, no. 4, pp. 713–730, 2016.

[24] S. K. Mitusch, S. W. Funke, and J. S. Dokken, "Dolfin-adjoint 2018.1: Automated adjoints for fenics and firedrake," *Journal of Open Source Software*, vol. 4, no. 38, p. 1292, 2019.